

LETTER TO THE EDITOR

A candidate quadruple AGN system at $z \sim 3$

Eileen Herwig¹, Fabrizio Arrigoni Battaia¹, Eduardo Bañados², and Emanuele P. Farina³

¹ Max-Planck-Institut für Astrophysik, Karl-Schwarzschild-Straße 1, D-85748 Garching bei München, Germany
e-mail: eherwig@mpa-garching.mpg.de

² Max Planck Institut für Astronomie, Königstuhl 17, D-69117, Heidelberg, Germany

³ International Gemini Observatory, NSF's NOIRLab, 670 N A'ohoku Place, Hilo, Hawai'i 96720, USA

October 3, 2024

ABSTRACT

Multiple galaxies hosting active galactic nuclei (AGNs) at kpc separation from each other are exceedingly rare, and in fact, only one quadruple AGN is known so far. These extreme density peaks are expected to pinpoint protocluster environments and therefore be surrounded by large galaxy overdensities. In this letter, we present another quadruple AGN candidate at $z \sim 3$ including two SDSS quasars at a separation of roughly 480 kpc. The brighter quasar is accompanied by two AGN candidates (a type 1 AGN and a likely type 2 quasar) at close (~ 20 kpc) separation identified through emission line ratios, line widths and high ionization lines like $N\text{v } \lambda 1240$. The extended $\text{Ly}\alpha$ emission associated with the close triple system is more modest in extent and brightness compared to similar multiple AGN systems and could be caused by ram-pressure stripping of the type-2 quasar host during infall into the central dark matter halo. The projected evolution of the system into a $z = 0$ galaxy cluster with the AGN host galaxies forming the brightest cluster galaxy needs to be further tested by galaxy overdensity studies on large scales around the quadruple AGN candidate. If confirmed as a quadruple AGN with X-ray observations or rest-frame optical line ratios, this system would represent the second AGN quartet, the highest-redshift multiplet and the closest high-redshift triplet known.

Key words. Galaxies: clusters: general – Galaxies: evolution – quasars: general

1. Introduction

In recent years, efforts to identify the progenitors of galaxy clusters, so called protoclusters (e.g., Overzier 2016), have accelerated. Protoclusters in simulations are simply defined as structures eventually coalescing into a virialized galaxy group of mass $M > 10^{14} M_{\odot}$ at $z = 0$. Observationally, the identification of protoclusters is more complicated. High- z quasars have long been believed to be signposts of peaks in the density distribution, but remain controversial as a method to identify protoclusters (Uchiyama et al. 2018; Habouzit et al. 2019). While they often do reside in overdensities (Fossati et al. 2021; García-Vergara et al. 2022), their typical halo masses of $10^{12.5} M_{\odot}$ at $z \sim 3$ are much lower than cluster masses (White et al. 2012; Trainor & Steidel 2012; Husband et al. 2013), requiring substantial growth to form a galaxy cluster until $z = 0$.

While single bright quasars may pinpoint protocluster cores, physically associated multiple AGN systems could be even more reliable tracers of local overdensities (Onoue et al. 2018; Sandrinelli et al. 2018), albeit also not a firm indicator (Fukugita et al. 2004; Green et al. 2011), as a number of highly active, massive galaxies require ample supply of cold gas feeding supermassive black holes (SMBHs) and star formation. In the framework of hierarchical structure formation, such objects are most likely to reside in peaks of the density field populating the rare massive end of the halo mass function (Bhowmick et al. 2020). In the absence of dense environments, multiple AGN systems would be exceedingly rare due to their transient nature (Hennawi et al. 2006).

Interactions of three SMBHs are also predicted to be almost always necessary to form ultra-massive black holes with black

hole masses $M_{\text{BH}} > 10^{10} M_{\odot}$ (Hoffman et al. 2023), further highlighting their importance in cluster formation as the central brightest cluster galaxies commonly host ultra-massive black holes (e.g., Dullo et al. 2017; Mehrgan et al. 2019).

So far, only a few multiple AGN systems on kiloparsec scales are known. These objects are likely in an early stage of galaxy merger and might share a dark matter halo, but not their host galaxies. In contrast to that, sub-arcsecond triple AGNs trace local late-stage mergers with multiple cores in the same host galaxy (e.g., Liu et al. 2011; Kalfountzou et al. 2017; Pfeifle et al. 2019). This work concentrates on the former AGN tuples on kiloparsec scales, of which only five are known.

Specifically, Hennawi et al. (2015) report the discovery of a quasar quartet at the peak of cosmic noon, $z \sim 2$. The AGN are embedded in a massive $\text{Ly}\alpha$ nebula extending by more than 300 kpc, indicative of a substantial reservoir of cool (10^4 K) gas ($\sim 10^{11} M_{\odot}$). The AGN are all found within a sphere of projected radius < 150 kpc. The first triple quasar to be identified also resides at a redshift of 2 within a projected distance of less than 50 kpc, consistent with the typical onset of AGN activity in galaxy mergers (Djorgovski et al. 2007). Another triplet has been detected at $z \sim 1.5$, consisting of a close pair with a companion at 200 kpc projected distance (Farina et al. 2013). The third triplet known is likewise embedded in a massive $\text{Ly}\alpha$ nebula at $z \sim 3$ and comprises two quasars and one faint AGN at projected distances below 100 kpc (Arrigoni Battaia et al. 2018). A fourth triplet was found in a sample of almost 20,000 AGN candidates at a redshift of 1.13 (Assef et al. 2018).

Here, we report on the discovery of a quadruple AGN candidate at $z \sim 3$ consisting of a close triplet, contained within 20 kpc in projection, and a fourth quasar at a separation of 478 kpc.

Throughout this work, we assume a flat Λ CDM cosmology with $H_0 = 67.7 \text{ km s}^{-1} \text{ Mpc}^{-1}$, $\Omega_m = 0.31$ and $\Omega_\Lambda = 0.69$ (Planck Collaboration et al. 2020). Reported quasar magnitudes are in the AB system.

2. Observation and Data Analysis

One quasar in the system, SDSS J101254.73+033548.7 (hereinafter QSO1), has been targeted with the Multi Unit Spectroscopic Explorer (MUSE; Bacon et al. 2010) on the Very Large Telescope as part of a survey to study the environment of quasar pairs (Herwig et al. 2024). QSO1 is a known member of a quasar pair from the SDSS DR12 (Pâris et al. 2017). The projected distance to the second quasar in the pair SDSS J101251.06+033616.5 (hereinafter QSO2) is 478 kpc. For QSO2, only the SDSS spectrum is available. Here we briefly describe the observations and data reduction. More detailed descriptions of sample selection, observation and subsequent data analysis can be found in Herwig et al. (2024). The MUSE data were acquired in Wide Field Mode on March 14, 2018 (seeing of $0.88''$), yielding a field of view (FoV) of $1' \times 1'$ (pixel scale of $0.2''$) and targeting only QSO1 as the separation of the pair is larger than the MUSE FoV. Three exposures were taken with 880 s on-source time each, rotated by 90 degrees with respect to each other and covering a wavelength range of $4750 \text{ \AA} - 9350 \text{ \AA}$ with a sampling of 1.25 \AA . The data have been reduced following Farina et al. (2019) and González Lobos et al. (2023). Specifically, we use the MUSE pipeline v 2.8.7 (Weilbacher et al. 2014, 2016, 2020) to perform bias- and sky-subtraction, flat fields, twilight and illumination correction and wavelength and flux calibration. To remove residual sky emission lines, we use the Zurich Atmospheric Purge (Soto et al. 2016). After masking gaps between the CCDs and correcting offsets between the exposures with custom routines, the three exposures are median combined to obtain the final data cube. To take into account correlated noise introduced during data processing, the variance cube produced by the pipeline is rescaled layer-by-layer to the RMS of a background region in the science cube, resulting in a mean pixel-wise noise level at the position of QSO1 of $4.6 \times 10^{-20} \text{ erg s}^{-1} \text{ cm}^{-2} \text{ \AA}^{-1}$.

3. Results

3.1. Discovery of a candidate quadruple AGN

By collapsing the final MUSE cube along the wavelength axis, we obtain a continuum image of the field surrounding QSO1. In this image (r-band in Fig. 1, left), two additional continuum sources are visible in close proximity to QSO1. While similar geometries can be seen as a result of gravitational lensing of a single source, we can confidently reject this possibility in this case (Appendix A). We instead identify both of these sources (hereinafter called AGNc1 and AGNc2) as AGN candidates as detailed in the following. To constrain their nature, we extract spectra from the MUSE cube within an aperture of $0.8''$ to minimize contamination from each other's PSFs. To determine their positions, we first model the PSF of a star within the MUSE FoV with a 2D Moffat function and fit the model to the three continuum sources observed with MUSE (QSO1, AGNc1, AGNc2) by fixing the FWHM and leaving amplitude and position free to vary (Fig.1, middle panel). The peak of the Moffat function is used as center of the aperture for spectral extraction and is indicated with pink circles (crosses) in the middle (right) panel of Fig. 1. To reduce noise while retaining the

signal, the spectra are smoothed by a 1D Gaussian kernel with $\sigma = 3$ pixels, corresponding to 3.75 \AA . Before smoothing the spectrum of AGNc2, a sky emission line at 6365.3 \AA is masked as it would otherwise be convolved with the $\text{C IV } \lambda 1550$ line. The spectra are shown in Fig. 2, together with the SDSS spectrum of QSO2. The two QSOs and two AGN candidates are all detected in $\text{Ly}\alpha$, confirming that they reside at roughly the same redshift. QSO1 and AGNc1 both show a broad $\text{C III] } \lambda 1908$ emission line, while in the spectrum of AGNc2, there is a tentative detection of a narrow $\text{C III] } \lambda 1908$ line as well as a prominent narrow, blue-shifted $\text{C IV } \lambda 1550$ line. A $\text{He II } \lambda 1640$ emission line is tentatively detected in all four objects. Within the aperture of $0.8''$ used for spectral extraction, the r -band magnitude for the three AGNs observed with MUSE is $m_{\text{QSO1}} = (22.56 \pm 0.11) \text{ mag}$, $m_{\text{AGNc1}} = (24.57 \pm 0.60) \text{ mag}$ and $m_{\text{AGNc2}} = (24.95 \pm 0.90) \text{ mag}$. In SDSS DR17 (Abdurro'uf et al. 2022), the r -band magnitude of QSO2 is reported as $m_{\text{QSO2}} = 21.65$. However, the SDSS fiber diameter of $3''$ is much larger than the aperture used in this work and consequently, the magnitude of QSO1 is reported to be much brighter in SDSS with $m_{\text{QSO1,SDSS}} = 21.89$. Between QSO1 and AGNc1, we measure an angular separation of $2.1''$, corresponding to the distance $\Delta d = 16 \text{ kpc}$ at this redshift. QSO1 and AGNc2 are separated by $2.6''$ or 20 kpc , and QSO2 is $61.6''$ or 478 kpc away from QSO1. We obtain the systemic redshift $z_{\text{CIII]}}$ by fitting the $\text{C III] } \lambda 1908$ line with a double Gaussian model and correcting by the characteristic velocity shift of -256 km s^{-1} between the peak of the line complex and the systemic redshift for quasars (Shen et al. 2016). The value obtained for AGNc1 is likely overestimated as a redshift of $z = 3.183$ implies a highly unusual $\text{Ly}\alpha$ line shape that is completely dominated by the blue wing (Fig. B.1). If this was the case, the $\text{He II } \lambda 1640$ line might be misidentified and possibly not detected. Positions of the AGN candidates and projected distance between each other as well as redshift and velocity shifts are summarized in Table 1.

We fit the spectra as described in Appendix B and summarize the resulting line fluxes, widths and upper flux limits in Table 2. Black hole mass estimates for QSO1 and QSO2 using the relation and absolute accuracy estimate derived for $\text{C IV } \lambda 1550$ in Vestergaard & Peterson (2006) are $\log M_{\text{BH,QSO1}} = (8.3 \pm 0.56) M_\odot$ and $\log M_{\text{BH,QSO2}} = (8.8 \pm 0.56) M_\odot$. The line width of AGNc2 is narrow with $\sigma = 243_{-18}^{+14} \text{ km s}^{-1}$ and consistent with a Type II AGN, while the spectrum of AGNc1 is dominated by broad lines of $\sigma = 1657_{-57}^{+46} \text{ km s}^{-1}$ indicative of a Type I AGN.

At the position of QSO1, radio emission is detected with a flux density of $f_{3\text{GHz}} = (0.7 \pm 0.1) \text{ mJy beam}^{-1}$ in VLASS (Lacy et al. 2020) and $f_{1.4\text{GHz}} = (1.02 \pm 0.15) \text{ mJy beam}^{-1}$ in VLA FIRST (Becker et al. 1994), leading to a radio slope of $\alpha = -0.49$ ($f_\nu \propto \nu^\alpha$). Additionally using the UV continuum slope from the fit to the spectrum of QSO1 (Appendix B) of $\beta = -1.04$ ($f_\lambda \propto \lambda^\beta$), we can calculate the ratio $R = f_{3\text{GHz}}/f_{4400\text{\AA}}$ (Kellermann et al. 1989) by extrapolating the rest-frame flux densities and obtain $R = 3078$, classifying QSO1 as radio-loud. Although no additional radio emission is detected, we cannot exclude that AGNc1 and AGNc2 are radio-loud due to the shallow surveys depth and their dim UV continuum.

3.1.1. Emission line diagnostics

A commonly adopted diagnostic diagram to distinguish AGNs from star forming galaxies (SFGs) in rest-frame UV uses the line ratios $\text{C IV } \lambda 1550/\text{C III] } \lambda 1908$ (C43), mainly influenced by the ionization parameter, and $\text{C III] } \lambda 1908/\text{He II } \lambda 1640$ (C3He2),

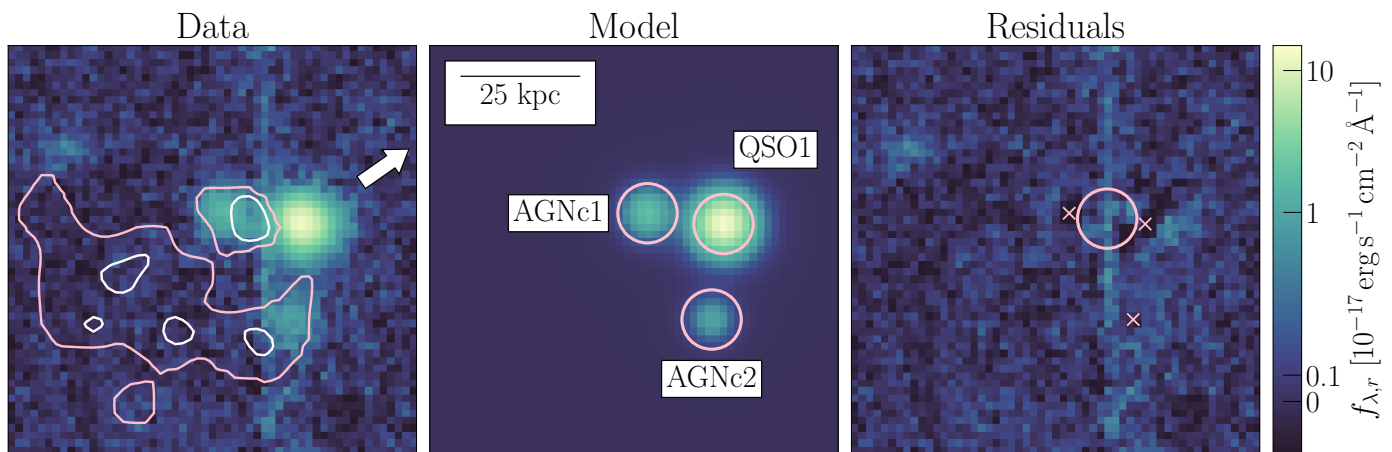


Fig. 1. **Left:** Extracted MUSE r -band map with overlaid the 2σ (pink) and 5σ (white) isophotes of extended Ly α emission associated with the system (Herwig et al. 2024). Shown is a cut-out of size $11'' \times 11''$. **Middle:** Best fitting Moffat model of the continuum sources. Pink circles indicate the apertures used for spectral extraction (Fig. 2). **Right:** Residual flux density after subtracting the model. The crosses show the centroid position of subtracted sources. The pink circle indicates the aperture used to calculate the maximum apparent magnitude of an interloping galaxy (if any).

Table 1. Quasar and AGN candidate properties and distances between each other.

Object	RA (J2000) ^a	Dec (J2000) ^a	r [mag] ^b	z_{CIII}	Δv to QSO1 [km s ⁻¹]	Δd to QSO1 ["/kpc]
QSO1	10:12:54.74	+03:35:48.93	22.56 ± 0.11	3.166 ± 0.001	0	0/0
AGNc1	10:12:54.88	+03:35:49.22	24.57 ± 0.60	3.183 ± 0.008	-1590 ± 766	2.1/16
AGNc2	10:12:54.77	+03:35:46.36	24.95 ± 0.90	3.158 ± 0.001	761 ± 166	2.6/20
QSO2	10:12:51.07 ^c	+03:36:16.56 ^c	21.65^d	3.152 ± 0.001	1347 ± 188	61.6/478

Notes. ^(a) Coordinates determined from best fitting Moffat model ^(b) Calculated in the MUSE data within an aperture diameter of $1.6''$ ^(c) Coordinate taken from SDSS ^(d) SDSS magnitude within an aperture of $3''$

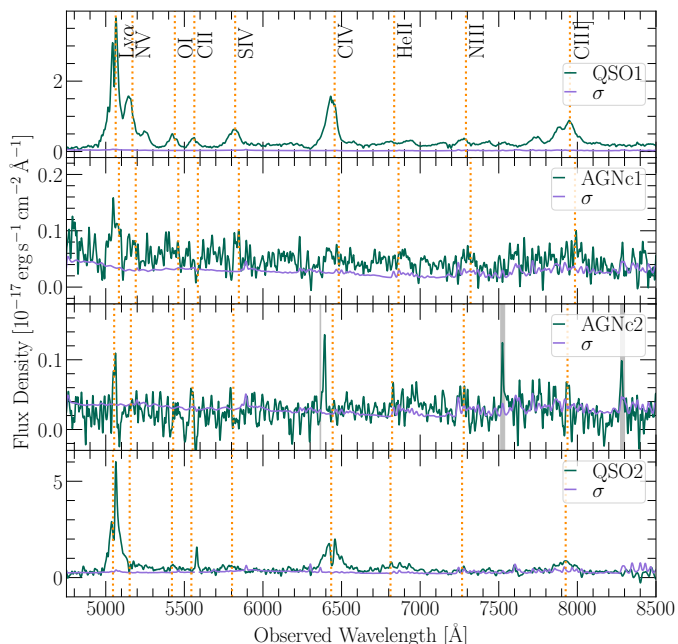


Fig. 2. One dimensional spectra for the candidate quadruple AGN system. QSO1 and QSO2 are the two SDSS quasars, while AGNc1 and AGNc2 are the two additional AGN candidates. For each source, we indicate both the data and noise spectrum (see legend). Orange dashed vertical lines indicates the location of important rest-frame UV transitions at the redshift of each object obtained from a fit to the C III] $\lambda 1908$ line. Location of sky-lines with residuals in the spectrum of AGNc2 are indicated with shaded vertical areas.

which is sensitive to metallicity and allows distinction between shocks and AGN photoionization (Feltre et al. 2016). Hirschmann et al. (2019) propose demarcation lines to distinguish between active and inactive galaxies, but current models are not capable of fully reproducing observed line ratios, leading to large impurities in the selection of AGNs and specifically faint AGNs. Classification is further complicated because certain types of galaxies would not appear in such a diagnostic diagram: high- z radio galaxies (HzRGs) commonly have no detection of C IV $\lambda 1550$ (56 % in De Breuck et al. 2000) and SFGs usually show C IV $\lambda 1550$ in absorption instead of emission (e.g. Shapley et al. 2003; Calabrò et al. 2022). In Fig. 3 we show the line ratios of the candidate AGNs and SDSS quasars together with line ratios of SFGs and different types of AGNs from the literature. Both quasars and both AGN candidates as well as 30 % of the literature AGNs fall within the composite region of the diagram, indicating contribution from both star formation and AGN activity. Surprisingly, the line ratios of QSO1 indicate the highest contribution from star formation of all four objects although it is definitively classified as quasar, further highlighting the difficulty in AGN selection based on UV line ratios. It is also notable that the stacks of observed SFGs selected based on C III] $\lambda 1908$ emission are classified as composite objects as well and show similar C3He2 ratios as AGNc1.

However, the detection of N V $\lambda 1240$ and the extreme line width of AGNc1 larger than 1500 km s^{-1} firmly point towards an AGN origin. If these broad lines were produced by galactic-scale outflows instead, the violent kinematics should lead to a high contribution from shocks and likely lead to a detectable C IV $\lambda 1550$ emission line.

Table 2. Line fluxes and line width.

Object	$f_{\text{Ly}\alpha}^a$	f_{NV}^a	f_{CIV}^a	f_{HeII}^a	f_{CIII}^a	σ [km s $^{-1}$]
QSO1 ^b	352.8 ± 9.3	44.4 ± 1.5	112.3 ± 0.9	17.3 ± 0.8	89.8 ± 0.9	2143 ± 23 ^d
AGNc1 ^c	36.9 ± 8.2	17.7 ± 1.4	<6.6	12.4 ± 3.9	39.0 ± 2.9	1657 ^{+46e} ₋₅₇
AGNc2 ^{c d}	19.3 ± 1.2	<1.5	13.2 ± 1.6	3.5 ± 0.6	13.8 ± 4.6	243 ^{+14f} ₋₁₈
QSO2 ^b	272.2 ± 9.1	-	159.9 ± 7.8	47.1 ± 7.1	71.6 ± 8.1	2121 ± 289 ^d

Notes. (a) Line flux in 10 $^{-17}$ erg s $^{-1}$ cm $^{-2}$ (b) Values obtained from pyQSOFIT (c) Flux values obtained by Gaussian fitting, line width σ obtained from the second moment (d) Line width determined from C III] λ 1908 (e) Line width determined from Ly α (f) Line width determined from C IV λ 1550

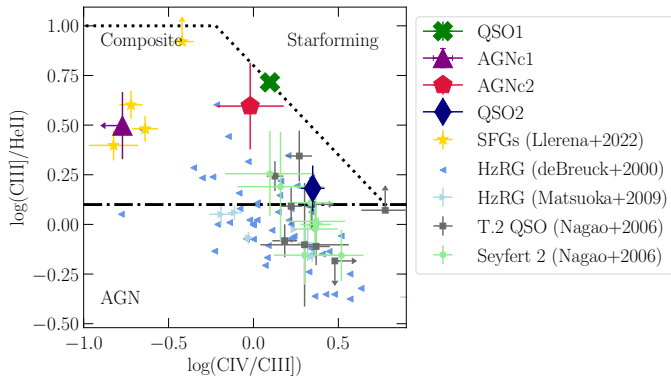


Fig. 3. Diagnostic diagram based on the line ratios C IV λ 1550/C III] λ 1908 and C III] λ 1908/He II λ 1640. Demarcation lines between AGN, star forming galaxies and composite line ratios are taken from Hirschmann et al. (2019). The values for QSO1, AGNc1, AGNc2 and QSO2 are compared to literature values for different types of galaxies: C III] λ 1908-selected starforming galaxies at $z > 2.9$ binned by stellar mass (Llerena et al. 2022), high- z radio galaxies with detections in all lines (De Breuck et al. 2000; Matsuoka et al. 2009), high- z X-ray selected type 2 quasars (Nagao et al. 2006) and local Seyfert 2 AGNs (Nagao et al. 2006).

4. Discussion

4.1. Clues from the peculiar extended Ly α emission

The pink contours in Fig. 1 show the 2σ and 5σ levels of extended Ly α emission, corresponding to a surface brightness of 3.0×10^{-18} erg s $^{-1}$ cm $^{-2}$ arcsec $^{-2}$ and 7.4×10^{-18} erg s $^{-1}$ cm $^{-2}$ arcsec $^{-2}$ respectively, and determined after subtracting empirical quasar point spread functions and continuum sources from the combined cube. This analysis is described in detail in Herwig et al. (2024) and Lobos et al. (2023). The nebular emission extends for about 50 kpc in the south-east direction with respect to QSO1, starting from the projected location of AGNc2. Additional Ly α emission coincides with the position of AGNc1. Surprisingly, the surface brightness level of the extended Ly α emission is much lower than typically found for multiple AGN systems (Hennawi et al. 2015; Arrigoni Battaia et al. 2018) and the AGN candidates are not embedded in the nebula. Instead, the flux-weighted centroid of the extended emission is offset from QSO1 by 34 kpc (Herwig et al. 2024). Possible explanations for this could be a faster evolution and therefore early cool gas depletion of outlier density peaks in the universe or a later merger stage of the close AGN triplet candidate presented in this work. Moreover, strong feedback effects might have already depleted the circumgalactic medium of this system of cool gas.

The peculiar morphology of the extended Ly α emission could be further evidence for violent on-going galaxy interactions: if the ISM of AGNc2 is ram-pressure stripped during the infall into the hot halo of QSO1, the trailing dense gas behind AGNc2 could become visible as extended Ly α emission. Indeed, estimating the stripped gas mass yields a lower limit of at least $6.3 \times 10^9 M_{\odot}$ when assuming the line-of-sight velocity, or roughly $8.6 \times 10^9 M_{\odot}$ when using a conservative estimate of the 3D velocity, while the estimated cool gas mass visible as extended Ly α emission amounts to roughly $4.8 \times 10^9 M_{\odot}$ (Appendix C). This first estimate confirms that ram-pressure stripping could be an effective mechanism in this configuration and could indeed explain the peculiar appearance of the extended Ly α emission. Evidence for similar ram-pressure stripping events around high- z quasars have been recently invoked by other studies on extended Ly α emission (e.g., Chen et al. 2021).

4.2. Evolutionary scenario

The close separation of QSO1, AGNc1 and AGNc2 and evidence for gas stripping and therefore ongoing galaxy interactions makes it very likely that the host galaxies will quickly merge into one massive galaxy. The result of such a merger is predicted to have a host halo mass of $10^{13} M_{\odot}$ (Bhowmick et al. 2020). Three-body interactions have a high likelihood of ejecting one of the participants via gravitational recoil (Partmann et al. 2024). This is the most probable evolution of the close black hole system, although two or even three mergers are also possible and would lead to the emission of gravitational waves possibly contributing to the gravitational wave background (Sesana et al. 2008) and likely the formation of an ultra-massive ($M_{\text{BH}} > 10^{10} M_{\odot}$) black hole. However, ejection or stalling of one or two black holes is predicted to not hinder fast growth: in simulations, the strong gravitational forces lead to quick infall times of gas into the most massive black hole and facilitate black hole mass growth up to $10^{10} M_{\odot}$ irrespective of coalescence (Hoffman et al. 2023). The extreme density peak implied by the presence of four AGNs in close proximity and three AGNs in the same dark matter halo is likely accompanied by a galaxy overdensity. This hypothesis needs to be tested by multi-wavelength observations targeting the galaxy population on Mpc scales around the quadruple AGN candidate. If confirmed, the most probable evolutionary path of this extraordinary system is the formation of a galaxy cluster in which the brightest cluster galaxy is formed out of the close triple AGN host galaxies.

4.3. Incidence rate of AGN tuples

Following Hennawi et al. (2015), an estimate of the probability to find such two close companion AGNs to a known quasar can be gained from the two-point correlation function for quasars

and amounts to $\sim 10^{-8}$, or $\sim 10^{-5}$ if considering any halo-scale triple AGN (Appendix D). A different generalized estimate for the AGN tuple incidence rate can be gained by considering the full observed parent sample. Including the candidate presented in this work, 2 AGN tuples have been identified within the QSO MUSEUM survey encompassing 134 quasars at $3 < z < 4$ observed with MUSE to similar depths (Arrigoni Battaia et al. 2019; Herwig et al. 2024; González Lobos et al. in preparation). This corresponds to an incidence rate of such systems of $1.5_{-1}^{+1.9} \%$ with Poisson errors for small-numbers statistics from Gehrels (1986), much larger than the above calculations and than previously believed (Hennawi et al. 2015). This implies 511_{-341}^{+647} undiscovered tuple systems around SDSS quasars (Pâris et al. 2018) in the same redshift range (with a median redshift of $z = 3.226$), and, extrapolated to the entire sky, 2810_{-1873}^{+3559} AGN tuples. Assuming that black hole tuples populate the massive end of the halo mass function and that 65 % of them are visible as AGN tuples (Hoffman et al. 2023), this number would amount to all halos down to $M_{\text{vir}} = (5 \pm 1) \times 10^{13} M_{\odot}$ of the $z = 3.226$ halo mass function (Behroozi et al. 2013).

5. Summary

We present an unlensed candidate quadruple AGN system at $z \sim 3$ consisting of two SDSS type 1 quasars at a separation of roughly 480 kpc (QSO1 and QSO2) and two AGN candidates (AGNc1 and AGNc2) accompanying QSO1 in close proximity with a projected separation of up to 20 kpc. The identification as probable AGN candidates is based on C43 versus C4He2 line ratios, high ionization lines like $N \text{ v } \lambda 1240$ in their spectrum and the emission line widths. AGNc1 is a potential type 1 AGN, while the spectral characteristics of AGNc2 align with those of a type 2 quasar. Further observations in X-ray or of rest-frame optical lines can confirm these objects as AGNs and allow for more reliable redshift determination.

The close triple system (QSO1, AGNc1, AGNc2) is associated with a Ly α nebula, although it is not embedded within it. A possible explanation for the presence of peculiar Ly α -bright gas is ram-pressure stripping of AGNc2 during its infall into the halo of QSO1.

This extraordinary system likely pinpoints a site of galaxy cluster formation. This hypothesis needs to be tested further by studying the Mpc-scale galaxy overdensity surrounding the quadruple AGN candidate.

This new candidate quadruple AGN allow us to refine the incidence rate of such rare systems around $z \sim 3$ SDSS quasars to $1.5_{-1}^{+1.9} \%$. Pre-selection of SDSS quasars with close faint sources (e.g., Euclid) is essential to build a statistical sample (12 systems), needed to confirm our statistics and constrain current models (e.g., Hoffman et al. 2023). Without it, additional 700_{-218}^{+1566} MUSE observations (1 hour/source) of SDSS quasars would be required.

Acknowledgements. We thank Guinevere Kauffmann for providing useful comments to this work. E.P.F. is supported by the international Gemini Observatory, a program of NSF NOIRLab, which is managed by the Association of Universities for Research in Astronomy (AURA) under a cooperative agreement with the U.S. National Science Foundation, on behalf of the Gemini partnership of Argentina, Brazil, Canada, Chile, the Republic of Korea, and the United States of America.

References

Abdurro'uf, Accetta, K., Aerts, C., et al. 2022, *ApJS*, 259, 35
 Agnello, A., Lin, H., Kuroptkin, N., et al. 2018, *MNRAS*, 479, 4345

Arrigoni Battaia, F., Chen, C.-C., Liu, H.-Y. B., et al. 2022, *ApJ*, 930, 72
 Arrigoni Battaia, F., Hennawi, J. F., Prochaska, J. X., et al. 2019, *MNRAS*, 482, 3162
 Arrigoni Battaia, F., Prochaska, J. X., Hennawi, J. F., et al. 2018, *MNRAS*, 473, 3907
 Assef, R. J., Stern, D., Noirot, G., et al. 2018, *ApJS*, 234, 23
 Bacon, R., Accardo, M., Adjali, L., et al. 2010, in *Society of Photo-Optical Instrumentation Engineers (SPIE) Conference Series*, Vol. 7735, Ground-based and Airborne Instrumentation for Astronomy III, ed. I. S. McLean, S. K. Ramsay, & H. Takami, 773508
 Becker, R. H., White, R. L., & Helfand, D. J. 1994, in *Astronomical Society of the Pacific Conference Series*, Vol. 61, *Astronomical Data Analysis Software and Systems III*, ed. D. R. Crabtree, R. J. Hanisch, & J. Barnes, 165
 Behroozi, P. S., Wechsler, R. H., & Conroy, C. 2013, *ApJ*, 770, 57
 Bhowmick, A. K., Di Matteo, T., & Myers, A. D. 2020, *MNRAS*, 492, 5620
 Calabrò, A., Pentericci, L., Talia, M., et al. 2022, *A&A*, 667, A117
 Chen, C.-C., Arrigoni Battaia, F., Emonts, B. H. C., Lehnert, M. D., & Prochaska, J. X. 2021, *ApJ*, 923, 200
 De Breuck, C., Röttgering, H., Miley, G., van Breugel, W., & Best, P. 2000, *A&A*, 362, 519
 Djorgovski, S. G., Courbin, F., Meylan, G., et al. 2007, *ApJ*, 662, L1
 Dullo, B. T., Graham, A. W., & Knapen, J. H. 2017, *MNRAS*, 471, 2321
 Farina, E. P., Arrigoni-Battaia, F., Costa, T., et al. 2019, *ApJ*, 887, 196
 Farina, E. P., Montuori, C., Decarli, R., & Fumagalli, M. 2013, *MNRAS*, 431, 1019
 Feltre, A., Charlot, S., & Gutkin, J. 2016, *MNRAS*, 456, 3354
 Fossati, M., Fumagalli, M., Lofthouse, E. K., et al. 2021, *MNRAS*, 503, 3044
 Fukugita, M., Nakamura, O., Schneider, D. P., Doi, M., & Kashikawa, N. 2004, *ApJ*, 603, L65
 García-Vergara, C., Rybak, M., Hodge, J., et al. 2022, *ApJ*, 927, 65
 Gehrels, N. 1986, *ApJ*, 303, 336
 González Lobos, V., Arrigoni Battaia, F., Chang, S.-J., et al. 2023, *A&A*, 679, A41
 Green, P. J., Myers, A. D., Barkhouse, W. A., et al. 2011, *ApJ*, 743, 81
 Gunn, J. E. & Gott, J. Richard, I. 1972, *ApJ*, 176, 1
 Guo, H., Shen, Y., & Wang, S. 2018, *PyQSOFit*: Python code to fit the spectrum of quasars, *Astrophysics Source Code Library*, record ascl:1809.008
 Habouzit, M., Volonteri, M., Somerville, R. S., et al. 2019, *MNRAS*, 489, 1206
 Hennawi, J. F., Prochaska, J. X., Cantalupo, S., & Arrigoni-Battaia, F. 2015, *Science*, 348, 779
 Hennawi, J. F., Strauss, M. A., Oguri, M., et al. 2006, *AJ*, 131, 1
 Herwig, E., Arrigoni Battaia, F., González Lobos, J., et al. 2024, *arXiv e-prints*, arXiv:2408.16826
 Hirschmann, M., Charlot, S., Feltre, A., et al. 2019, *MNRAS*, 487, 333
 Hoffman, C., Chen, N., Di Matteo, T., et al. 2023, *MNRAS*, 524, 1987
 Husband, K., Bremer, M. N., Stanway, E. R., et al. 2013, *MNRAS*, 432, 2869
 Kalfountzou, E., Santos Lleo, M., & Trichas, M. 2017, *ApJ*, 851, L15
 Kayo, I. & Oguri, M. 2012, *MNRAS*, 424, 1363
 Kellermann, K. I., Sramek, R., Schmidt, M., Shaffer, D. B., & Green, R. 1989, *AJ*, 98, 1195
 Kocevski, D. D., Barro, G., McGrath, E. J., et al. 2023, *ApJ*, 946, L14
 Lacy, M., Baum, S. A., Chandler, C. J., et al. 2020, *PASP*, 132, 035001
 Lau, M. W., Prochaska, J. X., & Hennawi, J. F. 2016, *ApJS*, 226, 25
 Liu, X., Shen, Y., & Strauss, M. A. 2011, *ApJ*, 736, L7
 Llerena, M., Amorín, R., Cullen, F., et al. 2022, *A&A*, 659, A16
 Lobos, V. G., Arrigoni Battaia, F., Chang, S.-J., et al. 2023, *A&A*, 679, A41
 Matsuoka, K., Nagao, T., Maiolino, R., Marconi, A., & Taniguchi, Y. 2009, *A&A*, 503, 721
 Mehran, K., Thomas, J., Saglia, R., et al. 2019, *ApJ*, 887, 195
 Nagao, T., Maiolino, R., & Marconi, A. 2006, *A&A*, 447, 863
 Nigoche-Netro, A., Aguerri, J. A. L., Lagos, P., et al. 2010, *A&A*, 516, A96
 Onoue, M., Kashikawa, N., Uchiyama, H., et al. 2018, *PASJ*, 70, S31
 Overzier, R. A. 2016, *A&A Rev.*, 24, 14
 Pâris, I., Petitjean, P., Aubourg, E., et al. 2018, *A&A*, 613, A51
 Pâris, I., Petitjean, P., Ross, N. P., et al. 2017, *A&A*, 597, A79
 Partmann, C., Naab, T., Rantala, A., et al. 2024, *MNRAS*, 532, 4681
 Pfeifle, R. W., Satyapal, S., Manzano-King, C., et al. 2019, *ApJ*, 883, 167
 Planck Collaboration, Aghanim, N., Akrami, Y., et al. 2020, *A&A*, 641, A6
 Runnøe, J. C., Brotherton, M. S., & Shang, Z. 2012, *MNRAS*, 422, 478
 Sandrinelli, A., Falomo, R., Treves, A., Scarpa, R., & Uslenghi, M. 2018, *MNRAS*, 474, 4925
 Sesana, A., Vecchio, A., & Colacino, C. N. 2008, *MNRAS*, 390, 192
 Shapley, A. E., Steidel, C. C., Pettini, M., & Adelberger, K. L. 2003, *ApJ*, 588, 65
 Shen, X., Hopkins, P. F., Faucher-Giguère, C.-A., et al. 2020, *MNRAS*, 495, 3252
 Shen, Y., Brandt, W. N., Richards, G. T., et al. 2016, *ApJ*, 831, 7
 Shen, Y., Hall, P. B., Horne, K., et al. 2019, *ApJS*, 241, 34
 Soto, K. T., Lilly, S. J., Bacon, R., Richard, J., & Conseil, S. 2016, *MNRAS*, 458, 3210

- Trainor, R. F. & Steidel, C. C. 2012, *ApJ*, 752, 39
- Uchiyama, H., Toshikawa, J., Kashikawa, N., et al. 2018, *PASJ*, 70, S32
- Vestergaard, M. & Peterson, B. M. 2006, *ApJ*, 641, 689
- Virtanen, P., Gommers, R., Oliphant, T. E., et al. 2020, *Nature Methods*, 17, 261
- Ward, E., de la Vega, A., Mobasher, B., et al. 2024, *ApJ*, 962, 176
- Weilbacher, P. M., Palsa, R., Streicher, O., et al. 2020, *A&A*, 641, A28
- Weilbacher, P. M., Streicher, O., & Palsa, R. 2016, MUSE-DRP: MUSE Data Reduction Pipeline, Astrophysics Source Code Library, record ascl:1610.004
- Weilbacher, P. M., Streicher, O., Urrutia, T., et al. 2014, in *Astronomical Society of the Pacific Conference Series*, Vol. 485, *Astronomical Data Analysis Software and Systems XXIII*, ed. N. Manset & P. Forshay, 451
- White, M., Myers, A. D., Ross, N. P., et al. 2012, *MNRAS*, 424, 933
- Wijers, N. A. & Schaye, J. 2022, *MNRAS*, 514, 5214

Appendix A: Rejecting the possibility of gravitational lensing

A possible explanation for multiple quasars in close separation is gravitational lensing of a single source (e.g., Agnello et al. 2018). In this case, the spectra would be very similar with slight variations due to different light paths. While all AGN in this system appear to have significantly different spectra (Fig. 2), this view might be skewed by the low signal to noise ratio of the fainter objects. While AGNc2 is a type 2 AGN candidate as it only shows narrow emission lines and should therefore be viewed at an entirely different angle than QSO1 and AGNc1, we explore the possibility that the latter two objects are actually two lensed images of the same quasar.

In this case, we expect to find a massive object capable of acting as the gravitational lens in between the two images. To calculate the necessary magnitude of a lensing elliptical galaxy, we follow Farina et al. (2013), making use of the Faber–Jackson relation by Nigoche-Netro et al. (2010) and assuming an isothermal sphere to link mass and velocity dispersion. Assuming an Einstein ring radius of $\Theta = 1.05''$, corresponding to half of the angular distance between QSO1 and AGNc1, the minimal possible apparent r -band magnitude of an interloper galaxy is $m = 21.6$ at $z \approx 1.89$, brighter than both the AGN candidates and QSO1.

We then inspect the residuals of the point spread function modeling (Fig. 1, right). There, an artifact of the CCD gap becomes apparent as vertical line, but no foreground galaxy is revealed. The r -band magnitude in a $1.6''$ aperture between QSO1 and AGNc1 (indicated as pink circle in Fig. 1, right) after masking negative values potentially arising due to the model subtraction is 26.6 mag, far below the faintest possible lensing galaxy. Therefore we conclude that no lensing geometry fits the observed pattern without revealing the lensing galaxy in the data cube.

Appendix B: Spectral fitting

We attempt to fit a set of rest-frame UV lines in the spectra of all four sources, namely $\text{Ly}\alpha$, $\text{N v } \lambda 1240$, $\text{C iv } \lambda 1550$, $\text{He II } \lambda 1640$ and $\text{C III] } \lambda 1908$. Due to the stark difference in magnitude and therefore data quality, we adopt two different methods. The two SDSS detected quasars QSO1 and QSO2 have sufficient S/N to be fitted using the package `pyQSOFIT` (Guo et al. 2018; Shen et al. 2019). We use the spectrum extracted from the MUSE cube as explained in Sec. 3.1 for QSO1 as it has higher S/N than the SDSS spectrum. For QSO2, only the SDSS spectrum is available. We smooth both by the same kernel size of $\sigma = 3$ pixels. Errors are estimated through 250 MCMC samplings, and the line width σ is determined from the fit to the $\text{C III] } \lambda 1908$ line. Although we attempt to include a component for the $\text{N v } \lambda 1240$ line when fitting the $\text{Ly}\alpha$ line complex of QSO2, we do not find a combination of priors that leads to convergence and we thus do not report a line flux for it. From `pyQSOFIT` we also obtain the continuum luminosity $L(1350\text{\AA})$ and the FWHM of $\text{C iv } \lambda 1550$ and use them to calculate black hole mass estimates for QSO1 and QSO2 using the relation and absolute accuracy estimate derived in Vestergaard & Peterson (2006). The obtained values are $\log M_{\text{BH,QSO1}} = (8.3 \pm 0.56) M_{\odot}$ and $\log M_{\text{BH,QSO2}} = (8.8 \pm 0.56) M_{\odot}$.

Due to the low S/N in the continuum, the line spectra of candidates AGNc1 (smoothed by a 1D Gaussian kernel with $\sigma = 5$ pixels; Fig. B.1) and AGNc2 (smoothed with $\sigma = 3$ pixels; Fig. B.2) instead are fitted with Gaussian or double Gaussian

line models and weighted by the noise spectra extracted from the rescaled variance cube. Fitting is performed using the function `curve_fit` in `scipy` (Virtanen et al. 2020).

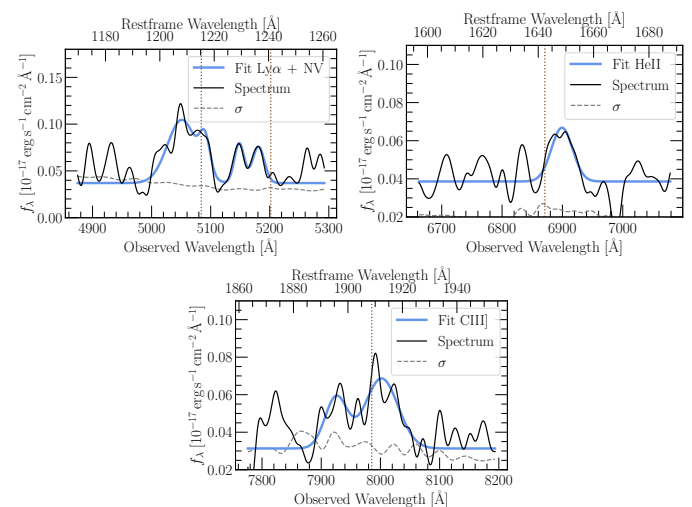


Fig. B.1. Gaussian fit to the emission lines in the spectrum of AGNc1, smoothed by a 1D Gaussian kernel with $\sigma = 5$ pixels. The vertical dotted brown line indicates the expected wavelength of the respective emission line, highlighting that the redshift determined from the peak of the $\text{C III] } \lambda 1908$ line complex could be overestimated and the $\text{He II } \lambda 1640$ line might be misidentified.

Due to the highly non-Gaussian $\text{Ly}\alpha$ line shape of AGNc1, the spectrum does not appear well-fit by the model. To test if this impacts the line flux, we smooth the spectrum further with a Gaussian kernel size of 10 pixels and repeat fitting. We find that the resulting line flux in both $\text{Ly}\alpha$ and $\text{N v } \lambda 1240$ is decreases by less than 4%. For the AGN candidates, the line widths σ are determined by calculating the second moment in an unsmoothed spectrum after subtracting the mean continuum level. The calculation window is chosen according to the width of the Gaussian line model fitted to the spectrum and centered on the $\text{Ly}\alpha$ line peak (AGNc1) and the $\text{C iv } \lambda 1550$ line peak (AGNc2). Although these lines are resonant and therefore not ideal for line width determination, they have the highest S/N and are the only lines

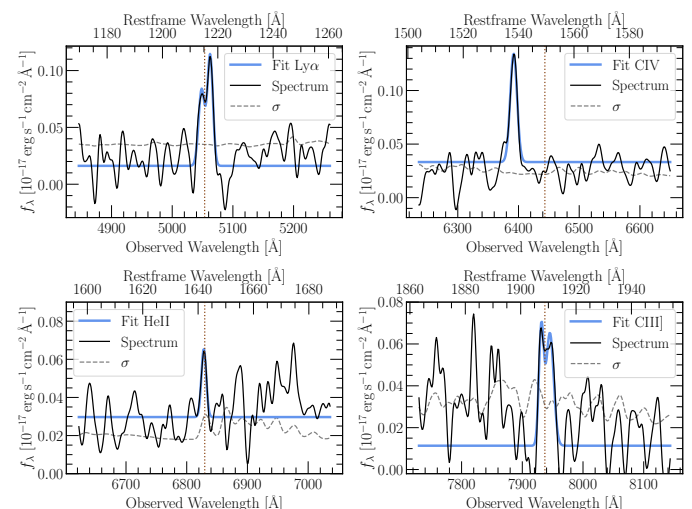


Fig. B.2. Same as Fig. B.1, but for AGNc2, smoothed by a 1D Gaussian kernel with $\sigma = 3$ pixels. The $\text{C iv } \lambda 1550$ line peak of the fit is blueshifted with respect to $z_{\text{C III]}}$ by -2395 km s^{-1} .

allowing for robust calculation of the second moment. Errors on σ are obtained by resampling the spectra with the associated noise spectra 10,000 times and, after calculating the second moment, the 25th and 75th percentiles of the obtained distribution are taken as lower and upper error.

A major source of uncertainty in the line flux of AGNc1 and AGNc2 is the poorly constrained underlying continuum. Especially the broad lines in the spectrum of AGNc1 are difficult to distinguish from the continuum and are affected by noise fluctuations, necessitating the large smoothing kernel size to be able to fit Gaussian profiles to the lines. Still, we can only place upper limits on C IV $\lambda 1550$ in the spectrum of AGNc1, and we also do not detect N V $\lambda 1240$ in the spectrum of AGNc2. Considering the large scatter in continuum level, we determine upper limits for the line fluxes by subtracting continuum implied by the minima closest to the expected line peak in the smoothed spectra and calculate moment 0 within 1σ left and right of the expected line peak.

Appendix C: Estimating the efficiency of ram pressure stripping

The peculiar extended Ly α emission associated with the close triple system might be a further indication of on-going galaxy interaction as the emission could be a result of ram-pressure stripped ISM of AGNc2 appearing Ly α bright. This could further explain the large velocity differences in the nebula obtained from the first moment with respect to AGNc2 (Fig. C.1), reaching 1500 km s^{-1} at the East edge of the isophote furthest away from the AGN candidate and generally approaching the systemic redshift of AGNc2 closer to it, although the nebula shows significant turbulence. To determine the feasibility of this hypothesis, we estimate the efficiency of stripping in the configuration of the system.

Ram-pressure stripping is possible if $\rho_{\text{halo}} v_{\text{AGNc2}}^2 > 2\pi G \sigma_s \sigma_g$ (Gunn & Gott 1972). In this, ρ_{halo} is the density of the hot gas in the halo of QSO1 and obtained from the typical volume-weighted number density in a hot halo of mass $\log(M/M_{\odot}) = 12.5 - 13$ at 20 % of the virial radius corresponding to the projected distance of AGNc2, $\log(n/[\text{cm}^{-3}]) = -3.9$ (Wijers & Schaye 2022). This mass bin is chosen as it includes the halo mass estimate for single quasars at this redshift ($10^{12.5} M_{\odot}$) as well as threefold this mass ($10^{13} M_{\odot}$) in case QSO1, AGNc1 and AGNc2 all share one dark matter halo and all three resided in quasar-typical massive halos before. This larger halo mass is also similar to that estimated for one of the known triplets (Arrigoni Battaia et al. 2022). v_{AGNc2} is the velocity with which AGNc2 is crossing the halo of QSO1 and at least as high as the line-of-sight velocity reported in Table 1. A conservative estimate of the 3D velocity is $v_{\text{AGNc2}} = \sqrt{3}\Delta v_{\text{AGNc2}} \approx 1318 \text{ km s}^{-1}$.

The gravitational pull of AGNc2 withstanding the ram pressure is described by the stellar and gas surface densities σ_s and σ_g . AGN hosts at $z \sim 3$ typically have a massive ($M_{\star} \sim 10^{11} M_{\odot}$), compact stellar component described by a Sersic profile with an average Sersic index of 2.6 and an effective radius of 0.9 kpc (Kocevski et al. 2023). The gas disk is well-described by an exponential profile, and we assume an effective radius of 2 kpc (Ward et al. 2024) and a cold gas mass fraction of 20 %. The stripped gas mass can then be estimated by integrating the gas mass profile beyond the radius at which ram pressure exceeds the gravitational pull of the galaxy, and it amounts to at least $6.3 \times 10^9 M_{\odot}$ when assuming the line-of-sight velocity, or roughly $8.6 \times 10^9 M_{\odot}$ when using the 3D velocity.

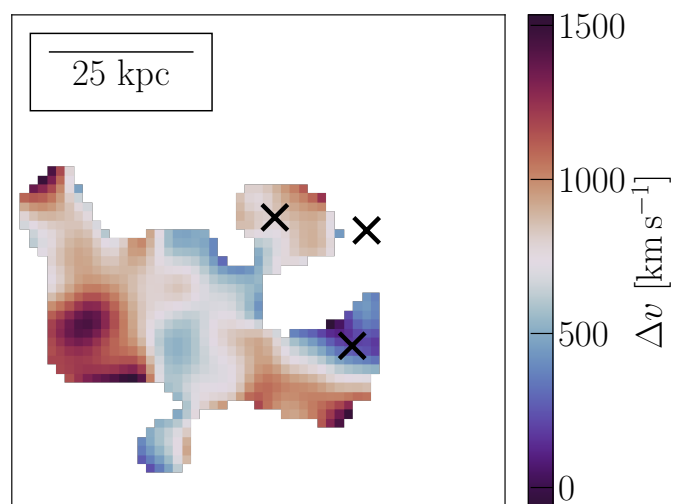


Fig. C.1. Moment 1 of the extended Ly α emission with respect to the systemic redshift of AGNc2. The centroid positions of QSO1, AGNc1 and AGNc2 are indicated with black crosses.

To contrast this with the Ly α -bright gas, we can estimate the mass from the extended emission using the equation $M_{\text{cool}} \sim AN_{\text{H}}m_p/X$ with the Ly α nebula area $A = 1437 \text{ kpc}^2$ (Herwig et al. 2024), the proton mass m_p and hydrogen fraction $X = 0.76$ and the typical CGM column density of cool gas, $\log(N_{\text{H}}/[\text{cm}^{-2}]) = 20.5$ (Lau et al. 2016). The latter quantity is associated with the highest uncertainty as it can vary by one order of magnitude and it might not be applicable to extraordinary systems. With these values, we obtain an estimated cool gas mass in the Ly α nebula of $4.8 \times 10^9 M_{\odot}$.

Appendix D: Probability of finding a similarly close AGN triple

The probability to find two additional AGNs close to a known quasar can be estimated using

$$P \sim 4 n_{\text{QSO}}^2 V \int_0^{r_{\text{max}}} \xi(r) 4\pi r^2 dr$$

with the comoving number density of AGNs n_{QSO} , the AGN-filled volume V , the maximum distance between the AGNs r_{max} and the two-point correlation function of quasars $\xi(r)$. This follows from a similar argument as presented in Hennawi et al. (2015), but we do not include the fourth object, QSO2, in the estimation as the large projected distance implies that QSO2 does not share a host halo with the other three objects (yet) and thus, other assumptions have to be made in the calculation. Specifically, in the case of a triplet, equation 2 in Hennawi et al. (2015) will only contain three permutations for the two-point correlation function and one permutation for the three-point correlation function. Although the three-point correlation function relates to ξ as $\zeta \sim \xi^{\frac{3}{2}}$ (Hennawi et al. 2015), in our order-of-magnitude estimation, we can approximate $\zeta \sim \xi$, hence the factor of four in the above probability equation.

We infer n_{QSO} from the quasar luminosity function at $z = 3$ (Shen et al. 2020) with a lower magnitude limit of $m_{\text{min},1450\text{\AA}} = 25 \text{ mag}$ and the quasar bolometric luminosity correction from Runnoe et al. (2012) resulting in $n_{\text{QSO}} = 9.3 \times 10^{-5} \text{ cMpc}^{-3}$. Due to the imprecision in redshift determinations from broad QSO emission lines and the possibility of high peculiar velocities

causing additional Doppler shifts, we extrapolate the maximum distance in the triplet, r_{\max} , as the highest projected distance plus a 50 % margin to account for projection effects. This yields a quasar-filled comoving volume of $V = 8 \times 10^{-3} \text{ cMpc}^3$. On small scales, the two-point correlation function is well described with $\xi = \left(\frac{r}{r_0}\right)^{-\gamma}$ with $\gamma = 2$ and $r_0 = 5.4 \pm 0.3 h^{-1} \text{ cMpc}$ (Kayo & Oguri 2012). Plugging in these values, we obtain $P \approx 3 \times 10^{-8}$.

The candidate triple AGN presented in this work is closer than previously found AGN triples. To get an estimate of the probability to find any AGN triple on halo scales, we repeat the calculation using $r_{\max} = 150 \text{ kpc}$, corresponding roughly to the virial radius of a halo with mass $10^{13} M_{\odot}$, and obtain a probability of $P \approx 2 \times 10^{-5}$. In contrast, the probability P_r to find three AGNs with $r_{\max} = 30 \text{ kpc}$ at random without considering clustering can be described with $P_r = n_{\text{QSO}}^2 \times V^2$ (Hennawi et al. 2015) and would be exceedingly rare with $P_r = 5.5 \times 10^{-13}$.